Measurement of partial muon capture rates in $1s$-$0d$ shell nuclei

T. P. Gorringe,[1] D. S. Armstrong,[2] S. Arole,[1] M. Boleman,[1,*] E. Gete,[3] V. Kuzmin,[4] B. A. Moftah,[3,†] R. Sedlar,[1,‡]
T. J. Stocki,[3,§] and T. Tetereva[5]

[1]*Department of Physics and Astronomy, University of Kentucky, Lexington, Kentucky 40506*
[2]*Department of Physics, College of William and Mary, Williamsburg, Virginia 23187*
[3]*Department of Physics and Astronomy, University of British Columbia, Vancouver, British Columbia, Canada V6T 1Z1*
[4]*Bogoliubov Laboratory of Theoretical Physics, Joint Institute for Nuclear Research, Dubna RU-141980, Russia*
[5]*Dubna Branch of Skobeltsyn Institute of Nuclear Physics, Lomonosov Moscow State University, Dubna RU-141980, Russia*

We report yields for 38 γ-ray lines and 29 (μ^-,ν) transitions following negative muon capture on ^{24}Mg, ^{28}Si, ^{31}P, and ^{32}S. Our results substantially increase the world data set for partial (μ^-,ν) transitions on $1s$-$0d$ shell nuclei. They also resolve a number of inconsistencies between previously published γ-ray yields and accepted γ-decay branching ratios. We compare the measured capture rates for the allowed Gamow-Teller (GT) transitions (supplemented with earlier ^{23}Na data) with a shell model calculation using the full $1s$-$0d$ space and universal SD interaction. We find a ''best fit'' value of the effective weak axial coupling of $\tilde{g}_a = -0.91^{+0.15}_{-0.17}$, fair agreement for the per-target summed GT capture rates, but poor agreement for the individual GT capture rates. By replacing the shell model $\sigma\tau^{\pm}$ matrix element values with experimentally determined $\sigma\tau^{\pm}$ matrix element values, improved predictions for the individual GT capture rates are obtained. Last, we comment on recent determinations of the weak coupling g_p via muon capture on $1s$-$0d$ shell nuclei.
[S0556-2813(99)05310-8]

PACS number(s): 23.40.Hc, 27.30.+t

I. INTRODUCTION

Nuclear muon capture and nuclear beta decay, $\mu^- + [A,Z] \rightarrow \nu + [A,Z-1]$ and $[A,Z] \rightarrow [A,Z\pm1] + e + \nu$, are examples of semileptonic charged-current weak interactions. Both processes are sensitive to the dynamics of the weak interaction and the structure of the atomic nucleus. However, while a great body of data exists for β decay, the data are sparse and spotty for μ^- capture.

A crucial difference between β decay and μ^- capture is their energy and momentum transfer. One consequence of the difference is a much greater role of the induced weak couplings (g_m and g_p) relative to the conventional weak couplings (g_a and g_v) in muon capture. Another consequence is the relatively broad spectrum of nuclear states populated in muon capture. These features make muon capture and β-decay studies complementary, for example, muon capture offering sensitivity to the induced pseudoscalar coupling g_p and accessibility to the Gamow-Teller (GT) resonance.

The nucleon's weak axial current is governed by two weak coupling constants: the axial coupling g_a and the induced pseudoscalar coupling g_p. For the free nucleon, the values of g_a and g_p embody how its weak interaction is dressed by its strong interaction. Here, the approximate chiral symmetry of light quark interactions leads to robust predictions for the coupling constants of $g_a = -1.23$ and $g_p = (6.7 \pm 0.18)$ g_a [1,2]. For the bound nucleon, additional modifications of the coupling constants due to nuclear medium effects are possible. Here, the effective weak axial and induced pseudoscalar couplings (denoted $\tilde{g}_a$ and $\tilde{g}_p$) can reveal the influence of non-nucleonic degrees of freedom such as meson exchange currents and Δ-hole excitations [3–5], and the partial restoration of chiral symmetry [6]. In particular, the coupling $\tilde{g}_p$ is a sensitive (albeit elusive) probe of these effects.

Interest in the medium modification of the coupling $\tilde{g}_p$ has motivated several recent experiments in nuclear muon capture. One experiment [7,8] measured hyperfine dependences for allowed GT transitions in μ^- ^{23}Na in order to determine $\tilde{g}_p$. Other experiments [9–11] measured angular correlations for allowed GT transitions in μ^- ^{28}Si in order to determine $\tilde{g}_p$. To extract $\tilde{g}_p$ from these data, the results have been analyzed with shell model calculations utilizing the full $1s$-$0d$ space and the universal SD interaction [7,8,12]. Curiously, while the ^{23}Na data yield $\tilde{g}_p = 6.5 \pm 2.4$ $\tilde{g}_a$ (i.e., consistent with the free nucleon prediction) the ^{28}Si data yield either $\tilde{g}_p = (-3 \pm 1.5)$ $\tilde{g}_a$, quoted in Ref. [13], or $\tilde{g}_p = (0 \pm 3.2)$ $\tilde{g}_a$ [11] (i.e., inconsistent with the free nucleon prediction).

An obvious question is the model sensitivity of the $\tilde{g}_p$ values extracted from the μ^- ^{23}Na hyperfine dependences and μ^- ^{28}Si angular correlations. An obvious test for the nuclear model is the muon capture rates for the relevant GT transitions. Generally, the μ^- capture rates for allowed GT transitions are dominated by the weak axial coupling and the $J_0(\nu r)\sigma\tau^{\pm}$ matrix element (for example see Ref. [14]). In

―――――――
*Present address: Department of Physics, University of South Alabama, Mobile, AL 36688.

†Present address: Department of Medical Physics, McGill University Health Center, Montreal, QC, Canada H3G 1A4.

‡Present address: The Boeing Company, Denver Engineering Center, 14261 E. 4th Ave., MC AG-00 Bldg. 6 Suite 100, Aurora, CO 80011.

§Present address: Digital Accelerator Corp., Suite 840, 650 W. Georgia, Box 11635, Vancouver, B.C., Canada V6B 4N9.

light of the puzzling results for the coupling $\tilde{g}_p$, a systematic study of capture rates for GT transitions in the $1s$-$0d$ shell, is clearly merited. In this article we report yields for 38 γ-ray lines and 29 (μ^-, ν) transitions following μ^- capture on $1s$-$0d$ nuclei. A systematic comparison of the measured rates (supplemented with earlier ^{23}Na data) with calculated rates is then conducted.

The article is organized as follows. The experimental setup is described in Sec. II and the determination of the γ-ray line and (μ^-, ν) transition yields are described in Sec. III. We compare our (μ^-, ν) data with earlier (μ^-, ν) data in Sec. IV B, and to shell model calculations of muon capture rates in Sec. IV C. The effects of replacing the shell model $\sigma\tau^{\pm}$ matrix element values with experimentally determined $\sigma\tau^{\pm}$ matrix element values is discussed in Sec. IV D. The topic of allowed GT transitions in μ^- ^{23}Na and μ^- ^{28}Si, and the determination of the effective value of the coupling $\tilde{g}_p$, is discussed in Sec. IV E.

II. EXPERIMENTAL SETUP

The experiment was conducted on the M9B beam line at the TRIUMF cyclotron. The beam line contains a 6 m, 1.2 T superconducting solenoid, into which 90 MeV/c pions were injected and from which 65 MeV/c backward-decay muons were extracted. The muon flux and spot size at the target location were defined by a lead collimator downstream of the beam pipe exit (the inner walls of the lead collimator were lined with polyethylene to reduce muon-induced x-ray, gamma-ray, and neutron backgrounds). After collimation the muon flux was 2×10^5 s^{-1}, spot size was approximately 5 cm$\times$5 cm, and e and π contaminations were $\sim 10\%$ and $<0.1\%$, respectively.

The targets were disks, approximately 6.0 cm in diameter and 1.0 cm in thickness, located 15 cm downstream of the collimator and angled at 45° to the beam axis (a compromise between maximizing the μ^- stop rate and minimizing the γ-ray absorption). The target materials were either granules or powders, which were sealed in cylindrical polyethylene containers with thin entrance and exit windows. For ^{24}Mg and ^{28}Si we used both elemental Mg and Si targets with natural (79% and 92%) isotopic abundances and oxide ^{24}MgO and ^{28}SiO$_2$ targets with enriched (99.90% and 99.71%) isotopic abundances. For ^{32}S we used both a natural (95%) isotopic abundance elemental target and an enriched (99.28%) isotopic abundance elemental target. For ^{31}P we used a natural (100%) isotopic abundance target.

A scintillator beam telescope was used for muon stop counting. The beam telescope comprised a plastic scintillator (S1) located between the beam pipe and the lead collimator, and a pair of plastic scintillators (S2 and S3) that sandwiched the target. The scintillators S1 and S3 were both 0.64 cm in thickness while the scintillator S2 was 0.16 cm in thickness (in order to minimize the miscounting of stops in the target material due to stops in the S2 scintillator).

To measure the γ-ray spectra following μ^- capture we used two high resolution Ge detectors (GeA and GeB). They were located at 90° to the beam axis and ~ 15 cm from the target center. GeA was a 40% n-type high-purity Ge crystal

with an in-beam energy resolution of 2.5 keV full width at half maximum (FWHM) and time resolution of 12 ns (FWHM) at 1.17 MeV. GeB was a 30% n-type high-purity Ge crystal with in-beam energy resolution of 2.1 keV (FWHM) and time resolution of 10 ns (FWHM) at 1.17 MeV. Surrounding the two Ge detectors (GeA and GeB) were two Compton suppressors (CSA and CSB) in order to reduce the continuum background in the Ge detectors due to Compton scattering. The suppressor CSA comprised a six-element NaI annulus with in-beam energy resolution of $\sim 10\%$ (FWHM) and time resolution of ~ 10 ns (FWHM) at 1.17 MeV. The suppressor CSB comprised a ten-element BGO cube [15] with in-beam energy resolution of $\sim 20\%$ (FWHM) and time resolution of ~ 10 ns (FWHM) at 1.17 MeV.

Valid gamma-ray events were defined by the ''OR'' of the two triggers GeA$\cdot\overline{\text{CSA}}\cdot\mu$STOP$\cdot\overline{\text{Busy}}$ and GeB$\cdot\overline{\text{CSB}}\cdot\mu$STOP$\cdot\overline{\text{Busy}}$, where GeA and GeB indicate a gamma-ray signal from the corresponding Ge detectors, $\overline{\text{CSA}}$ and $\overline{\text{CSB}}$ indicate the absence of signals from the corresponding Compton suppressors, μSTOP indicates a preceding muon stop, and $\overline{\text{Busy}}$ indicates the data acquisition system is live. The GeA (GeB) signal was defined by the coincidence GeAlo$\cdot$GeAhi (GeBlo$\cdot$GeBhi), where the ''lo'' and ''hi'' signals were derived from constant fraction discriminators (CFDs) on the Ge detector timing signals with low and high threshold settings. The low threshold CFD input defined the time of the valid Ge output, while the high threshold CFD input defined the ~ 300 keV low-energy cutoff of the valid Ge output. The CSA and CSB signals were defined by the ''ORs'' of CFD outputs corresponding to the six analog signals from the six-element suppressor CSA and the ten analog signals from the ten-element suppressor CSB, respectively. The low-energy cutoffs for the individual suppressor discriminator channels were set to ~ 400 keV and the $\overline{\text{CSA}}$ and $\overline{\text{CSB}}$ veto widths in the GeA$\cdot\overline{\text{CSA}}$ and GeB$\cdot\overline{\text{CSB}}$ anticoincidences were set to ~ 50 ns. Lastly, the μSTOP gate was defined by the output of a 2.0 μs updating gate generator fed by the logic signal S1$\cdot$S2$\cdot\overline{\text{S3}}$. The μSTOP gate was ''open'' whenever one or more muon stops were registered in the preceding 2.0 μs.

On receipt of a valid gamma-ray event, the data acquisition system read-out pulse height signals from the Ge detectors GeA and GeB, amplitude and timing signals from the Compton suppressors CSA and CSB and plastic scintillators S1, S2 and S3, and the times of the last four S1$\cdot$S2$\cdot\overline{\text{S3}}$ signals in the preceding 5.0 μs time interval (i.e., a beam history). Every ten seconds a scaler event recorded the scaler counts.

Table I summarizes the data taking runs on the various enriched and natural isotopic abundance ^{24}Mg, ^{28}Si, ^{31}P, and ^{32}S targets. Shorter muonic x-ray runs on Ca, Mn, Fe, Nb, In, and Pb targets were also performed for the energy calibration and the acceptance determination of the Ge detectors and Compton suppressors. Also, beam-on and beam-off ^{60}Co source data were collected for detector calibration and diagnostic purposes.

TABLE I. Summary of data collection. Columns 1–3 identify the target material and isotope abundance. Column 4 lists the muon stops per target material.

Target isotope	Isotopic abundance (%)	Chemical form	No. of muon stops ($\times 10^{10}$)
^{24}Mg	79	Mg	1.1
^{24}Mg	99.9	MgO	1.0
^{28}Si	92	Si	2.8
^{28}Si	99.7	SiO_2	0.5
^{31}P	100	red P	1.8
^{32}S	95	S	1.1
^{32}S	99.3	S	1.1

III. DATA ANALYSIS

A. Ge detector acceptance determination

To determine the acceptances $\epsilon\Delta\Omega_A$ and $\epsilon\Delta\Omega_B$ of the Ge detectors GeA and GeB we employed a variety of muonic x-ray lines from a number of convenient x-ray targets. For the target materials Mg, Si, P, S, Ca, Mn, and Nb we used their K-series muonic x rays which covered the energy range from 300 to 2600 keV. For the target materials Fe, In, and Pb we used their K- and L-series muonic x rays which covered the energy range from 250 to 6000 keV. In most cases published yield data for the individual muonic x rays were available for normalization purposes (method A). In a few cases we assumed a total K-series x-ray yield of unity for normalization purposes (method B). Table II compiles the muonic x-ray lines and published x-ray yield data [16–20] used in the acceptance determinations.

To compute the Ge detector acceptances from the muonic x-ray data we used the equation

$$\epsilon\Delta\Omega = \frac{N_x}{N_\mu Y_x} C_{ab} C_{sv} C_{bm}, \qquad (1)$$

TABLE II. Compilation of the muonic x-ray series and published muonic x-ray yields used for the Ge acceptance determinations. See text for the full explanation of the normalization methods A and B.

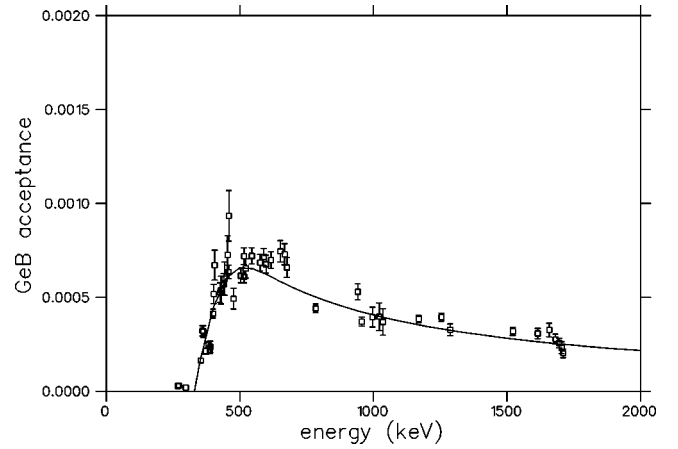| Atomic number	Target element	x-ray series	Energy range (keV)	Meth. of norm.	Ref.
12	Mg	$nP \to 1S$	298–391	A	[16]
14	Si	$nP \to 1S$	401–523	A	[17]
15	P	$nP \to 1S$	457–598	A	[16]
16	S	$nP \to 1S$	517–677	A	[16]
20	Ca	$nP \to 1S$	783–1034	A	[17]
25	Mn	$nP \to 1S$	1170–1560	B	
26	Fe	$nP \to 1S$	1255–1711	A	[18]
26	Fe	$nD \to 2P$	268–459	A	[18]
41	Nb	$nP \to 1S$	2614–3485	B	
49	In	$nD \to 2P$	954–1294	A	[19]
49	In	$nP \to 1S$	3344–4634	A	[19]
82	Pb	$2P_{1/2} \to 1S_{1/2}$	5766	A	[20]
82	Pb	$3D \to 2P$	2458–2643	A	[20]

FIG. 1. Ge acceptance versus photon energy for GeB. The data points are the measured acceptances using the muonic x-ray data and Eq. (1). The solid line is the ''best fit'' to the empirical energy dependence of Eq. (2).

where N_x is the number of muonic x-ray counts, N_μ is the number of livetime-corrected muon stops, and Y_x is the yield of either the individual x-ray (method A) or the complete x-ray series (method B). N_x was obtained from fits of Gaussian peaks to the x-ray line-shapes, N_μ from the scaler S1·S2·S3·$\overline{\text{Busy}}$, and Y_x from the references compiled in Table II. The factors C_{ab}, C_{sv}, and C_{bm} were minor corrections (i.e., $C \cong 1$), and are discussed in detail in the Appendix. The resulting values of the GeB detector acceptances are plotted in Fig. 1 (the GeA data are of similar quality). The error bars on the data points include the statistical uncertainties in the x-ray line-shape fit and the measurement uncertainties in the published x-ray yields.

To conveniently parametrize the detector acceptances, and their energy dependences, the muonic x-ray acceptance data were fit to the equation

$$\epsilon\Delta\Omega = \frac{a}{E+b} \, \text{erf}\left(\frac{E+c}{d}\right). \qquad (2)$$

In Eq. (2), E is the photon energy, the quotient (involving the parameters a and b) characterizes the decreasing Ge efficiency with increasing γ-ray energy, and the error function (involving the parameters c and d) characterizes the low-energy spectrum cutoff due to the discriminator threshold. The ''best fit'' curve $\epsilon\Delta\Omega_B$ is illustrated in Fig. 1. The ''best fit'' parameters a, b, c, and d for GeA and GeB are listed in Table III. The corresponding chi-squared values of 1.2 and 1.4 for Ge1 and Ge2 suggest additional uncertainties beyond the statistical errors in the data points (most likely due to target positioning and muon counting). Therefore, in computing the gamma-ray and state yields (see Secs. III C and III D), we accounted for additional systematic uncertainties by including an additional normalization error of $\pm 10\%$.

B. Gamma-ray line identification

The γ-ray spectra from each target typically contained 100–200 γ-ray lines, making the matching of measured

TABLE III. Quantities a, b, c, and d from the fit of Eq. (2) to the GeA and GeB x-ray acceptance determination data. The errors include the statistical uncertainties in the x-ray line-shapes and the experimental uncertainties in the published x-ray yields.

Parameter	GeA	GeB
a	0.730 ± 0.042	0.461 ± 0.025
b	275 ± 62 keV	137 ± 50 keV
c	248 ± 96 keV	330 ± 18 keV
d	172 ± 95 keV	143 ± 29 keV

γ-ray lines to known nuclear transitions quite a formidable task. Therefore, after determination of the energy calibrations of the Ge detectors, a semi-automated procedure was employed to match measured γ-ray energies with tabulated nuclear transitions.

To determine the energy calibrations of the Ge detectors we used approximately 20 muonic x rays and nuclear γ rays spanning the range from 300 to 6000 keV. The selection criteria for the calibration lines were solid identification, good statistics, low continuum background, no line backgrounds, and the absence of Doppler broadening of the γ-ray line-shape. For both GeA and GeB a linear fit between channel number and γ-ray energy was found to be perfectly adequate (i.e., no significant nonlinearities were found). For both GeA and GeB the rms deviations between the ''best fit'' and known photon energies were typically 0.3 keV.

In the first stage of the line identification procedure, we conducted an automated search, utilizing the energy level compilations of the NUDAT computer code [21], for matches between gamma-ray energies and nuclear transition energies following muon capture reactions of the type

$$\mu^- + [A,Z] \rightarrow [A-(x+y), Z-(x+1)]^* + \nu + xp + yn, \quad (3)$$
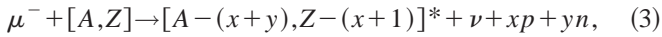
where $x, y = 0, 1, 2$. Matches were logged if (i) the γ-ray line energies and nuclear transition energies were within ± 2.0 keV, (ii) the γ-ray initial state was below 7000 keV, and (iii) the γ-ray final state was below 5000 keV (the excitation energy limits were picked to restrict the generation of large numbers of improbable matches).

Our general philosophy in the identification procedure was to retain only γ rays with robust identities and to reject any γ rays with problematic identities. In the second stage of the line identification procedure, we demanded consistency between the branching ratios and state lifetimes of Endt [22] and the observed γ-ray intensities and Doppler line-shapes of the first stage energy matches. In the $\mu^- {}^{24}$Mg data set, γ-ray peaks at 781 and 1344 keV, matching the 38% and 62% branches of the 1344 keV ^{24}Na level, were rejected because their Doppler widths were not consistent with the state lifetime. Also in the $\mu^- {}^{24}$Mg data set, a γ-ray peak at 2505 keV, matching the 24% decay branch of the 2978 keV ^{24}Na level, was rejected because a stronger 2414 keV γ-decay branch was absent. Lastly, hints of peaks at 1512 keV in the $\mu^- {}^{24}$Mg spectra (corresponding to the 100% decay branch of the 1512 keV ^{24}Na state), at 4815 keV in the $\mu^- {}^{28}$Si spectra (corresponding to a possible 4846→31 branch of the

4846 keV ^{28}Al state), and at 4259 keV in the $\mu^- {}^{31}$P spectra (corresponding to the 100% decay branch of the 4259 keV ^{31}Si state), were rejected due to poor signal-to-noise, peculiar line-shapes, or multiple candidates for the line origin.

The resulting data set of (μ^-, ν) induced gamma-ray lines consisted of six γ rays from six levels in ^{24}Na, nine γ rays from seven levels in ^{28}Al, nine γ rays from eight levels in ^{31}Si, and 14 γ rays from eight levels in ^{32}P. The observed γ-ray lines are listed in Table IV along with the energies and spin parities of the relevant initial and final states, and the γ-decay lifetimes and branching ratios (the spin parities, energies, lifetimes, and branching ratios were taken from the compilation of Endt [22]). In addition to the (μ, ν) induced gamma-ray lines of Table IV, many other gamma-ray lines from muon capture to particle unstable states are present in the data. These transitions will be discussed in a later publication.

C. Gamma-ray yield determinations

To determine the yields of the γ rays following muon capture we employed the equation

$$Y_\gamma = \frac{N_\gamma}{N_\mu \epsilon \Delta\Omega(E) f_{iso} f_{cap}} C_{bm} C_{lt} C_{ab} C_{sv}, \quad (4)$$

where N_γ is the number of γ-ray counts, N_μ is the number of lifetime corrected muon stops, $\epsilon\Delta\Omega(E)$ is the Ge detector acceptance at the gamma-ray energy, f_{iso} is the fraction of muons atomically captured by the particular target isotope, f_{cap} is the fraction of these muons that undergo nuclear capture, and the factors C_{bm}, C_{lt}, C_{ab}, and C_{sv} represent minor corrections that are described in the Appendix. The γ-ray counts N_γ were extracted from fits of either regular or Doppler-broadened Gaussian peaks to each gamma-ray line-shape. In these fits we fixed the peak centroids, instrumental widths and Doppler widths, and varied the peak and background amplitudes. In the case of the elemental Mg, Si, P, and S targets we used the fractional abundances of the mass 24, 28, 31, and 32 isotopes for the μ^- atomic capture fractions f_{iso}. In the case of the oxide ^{24}MgO and ^{28}SiO$_2$ targets we used the comparative yields of the Mg and Si muonic x rays from their elemental and oxide targets to compute the μ^- atomic capture fractions f_{iso}. The values of f_{cap} were taken from the muon disappearance rates of Suzuki *et al.* [24]. The livetime-corrected μ^- stops N_μ were obtained from the scalar $S1 \cdot S2 \cdot \overline{S3} \cdot \overline{Busy}$, and the detector acceptances $\epsilon\Delta\Omega_A(E)$ and $\epsilon\Delta\Omega_B(E)$ were obtained from Eq. (2) using the parameters in Table III. We stress that our definition of the gamma-ray yield Y_γ in Eq. (4) includes the production of γ rays both directly (i.e., μ^- capture occurring to the parent state) and indirectly (i.e., μ^- capture occurring to a higher lying state). We also stress that the γ-ray yield Y_γ in Eq. (4) is the yield per muon capture (not per muon stop).

The resulting γ-ray yields per muon capture following the (μ^-, ν) reactions on the targets ^{24}Mg, ^{28}Si, ^{31}P, and ^{32}S are listed in Table IV. The tabulated yields are the weighted averages of the GeA and GeB data obtained from the isoto-

TABLE IV. Measured γ-ray yields (Y_γ) per muon capture averaged from the GeA and GeB data. E_i, E_f and J_i^π, J_f^π are the initial and final state energies and spin parities, and E_γ, τ, and B are the γ-ray energy, lifetime, and branching ratio. Other than the γ-ray yield of the last column, the data are from Endt [22].

Final nucleus	E_i (keV)	J_i^π	E_f (keV)	J_f^π	E_γ (keV)	τ	B (%)	Y_γ ($\times 10^{-3}$)
^{24}Na	472	1^+	0	4^+	472	20.2 ms	100%	137.6±15.8
^{24}Na	1341	2^+	472	1^+	869	90 fs	95%	40.4±4.2
^{24}Na	1347	1^+	472	1^+	874	6.4 ps	100%	43.6±4.7
^{24}Na	1846	2^+	1347	1^+	499	260 fs	40%	2.8±0.4
^{24}Na	3372	2^-	1347	1^+	2025	19 fs	41%	3.2±0.4
^{24}Na	3413	1^+	1341	2^+	2074	<20 fs	43%	3.1±0.6
^{28}Al	972	0^+	31	2^+	941	48 ps	100%	29.6±3.6
^{28}Al	1372	1^+	31	2^+	1341	320 fs	55%	18.4±3.4
^{28}Al	1620	1^+	31	2^+	1588	120 fs	92%	15.1±2.2
^{28}Al	2138	2^+	31	2^+	2107	80 fs	52%	19.4±2.9
^{28}Al	2138	2^+	0	3^+	2138	80 fs	41%	26.3±3.8
^{28}Al	2201	1^+	972	0^+	1229	65 fs	16%	10.6±2.0
^{28}Al	2201	1^+	31	2^+	2171	65 fs	79%	62.6±6.8
^{28}Al	3105	1^+	31	2^+	3074	?	75%	12.7±2.2
^{28}Al	3876	2^-	0	3^+	3876	80 fs	79%	8.4±2.7
^{31}Si	752	$1/2^+$	0	$3/2^+$	752	760 fs	100%	60.5±6.7
^{31}Si	1695	$5/2^+$	0	$3/2^+$	1695	820 fs	100%	15.3±1.6
^{31}Si	2317	$3/2^+$	0	$3/2^+$	2317	55 fs	73%	7.2±0.8
^{31}Si	3133	$7/2^-$	1695	$5/2^+$	1439	540 fs	100%	2.6±0.3
^{31}Si	3534	$5/2^-$	752	$1/2^+$	2781	15 fs	95%	24.4±2.6
^{31}Si	4383	$3/2^-$	752	$1/2^+$	3629	?	76%	2.6±0.3
^{31}Si	4720	$1/2^+$	752	$1/2^+$	3966	?	?	19.6±2.0
^{31}Si	4720	$1/2^+$	0	$3/2^+$	4720	?	?	7.1±0.7
^{31}Si	5282	$1/2^+$	752	$1/2^+$	4528	?	100%	10.1±1.1
^{32}P	1149	1^+	513	0^+	636	253 fs	50%	15.9±1.8
^{32}P	1149	1^+	78	2^+	1071	253 fs	43%	12.6±1.4
^{32}P	1149	1^+	0	1^+	1149	253 fs	7.5%	2.1±0.2
^{32}P	1323	2^+	78	2^+	1244	472 fs	41%	7.5±0.8
^{32}P	1323	2^+	0	1^+	1323	472 fs	59%	12.0±1.3
^{32}P	1755	3^-	78	2^+	1676	660 fs	96%	6.3±0.7
^{32}P	2658	2^+	0	1^+	2658	<10 fs	69%	5.0±0.6
^{32}P	3264	2^-	1755	3^-	1508	130 fs	12%	4.7±0.5
^{32}P	3264	2^-	1323	2^+	1940	130 fs	18%	1.9±0.3
^{32}P	3264	2^-	1149	1^+	2114	130 fs	46%	10.0±1.0
^{32}P	3264	2^-	78	2^+	3185	130 fs	12%	3.7±0.4
^{32}P	3320	3^-	78	2^+	3242	260 fs	75%	4.4±0.5
^{32}P	4205	1^+	78	2^+	4126	?	100%	25.8±2.7
^{32}P	4710	1^+	78	2^+	4632	?	56%	8.0±0.9

pically enriched targets (the GeA and GeB results were mutually consistent within experimental uncertainties). The quoted errors include an overall normalization error of $\pm 10\%$ and the uncertainties from the γ-ray peak fitting and x-ray acceptance determination (the uncertainties in the various correction factors C_{ab}, C_{sv}, C_{bm}, and C_{lt} were negligible). To illustrate the computation of the γ-ray yield data, in Table V we give the values of the muon stops, detector acceptances, correction factors and resulting yields, for the example of the ^{32}S enriched target, GeA data set.

For the γ-ray yields in Table IV, we used the enriched target data rather than natural target data in order to eliminate the possibility of ($\mu^-, xn\nu$) induced γ rays from the heavier isotopes contaminating the (μ^-, ν) induced γ rays from the interesting isotopes. To assist in planning of future experiments (where for cost and/or convenience a natural target may be preferred to an enriched target), we note that the observed γ-ray lines with larger natural target than enriched target yields were the 499 and 2072 keV lines from ^{24}Mg, the 3876 keV line from ^{28}Si, and the 1676 and 1940 keV lines from ^{32}S. For these cases, the natural target γ-ray yields exceeded the enriched target γ-ray yields by 10–30%.

TABLE V. Illustrative data for the calculation of the γ-ray yields per muon capture (Y_γ) for μ^- ^{31}P, just for the GeA data set. Shown are the γ-ray counts (N_γ), livetime-corrected μ^- stops (N_μ), the GeA acceptance $\epsilon\Delta\Omega$, and the various correction factors C_{lt}, C_{bm}, C_{sv}, and C_{ab} used in Eq. (4).

γ-ray energy (keV)	N_γ ($\times 10^3$)	N_μ ($\times 10^{10}$)	C_{lt}	C_{bm}	C_{sv}	C_{ab}	$\epsilon\Delta\Omega$ ($\times 10^{-4}$)	Y_γ ($\times 10^{-3}$)
752	291.0	1.107	1.017	0.989	1.095	1.060	7.1	59.8
1695	35.1	1.107	1.017	0.989	1.091	1.039	3.7	13.5
2317	12.9	1.107	1.017	0.989	1.114	1.031	2.8	6.6
1439	6.4	1.107	1.017	0.989	1.127	1.041	4.3	2.2
2781	39.9	1.107	1.017	0.989	1.103	1.030	2.4	23.9
3629	3.0	1.107	1.017	0.989	1.101	1.028	1.9	2.3
3966	23.6	1.107	1.017	0.989	1.097	1.027	1.7	19.4
4720	8.5	1.107	1.017	0.989	1.101	1.026	1.5	8.2
4528	11.9	1.107	1.017	0.989	1.084	1.026	1.5	11.0

D. State yield determination

The μ^- capture induced γ rays in Table IV may be produced both directly, via muon capture to the γ-ray parent state, or indirectly, via muon capture to a higher-lying state. In discussing the state yield following muon capture we therefore distinguish the direct yield of state S due to muon capture to state S (denoted Y_S^S), the indirect yield of state S due to muon capture to state S' (denoted $Y_S^{S'}$), and the total (direct and indirect) yield of state S (denoted Y_S). To compute the direct state yields, we first determined the total state yields, and then subtracted the indirect state yields.

The total state yields Y_S for the various states S were obtained using

$$Y_S = \frac{\Sigma Y_\gamma}{\Sigma B} \qquad (5)$$

and the γ-ray yield data of Table IV. In Eq. (5), Y_γ and B are the measured γ-ray yields and corresponding γ-ray branching ratios [22] for the observed γ rays. The summations are over all observed γ decays from the particular parent state S.

We then subtracted both ''observed feeding'' and ''inferred feeding'' from the total state yield Y_S of Eq. (5) to obtain the direct state yield Y_S^S. In the case of observed feeding, the feeding γ ray was observed in our γ-ray spectra, and γ-ray yield is listed in Table IV. In the case of inferred feeding, the feeding γ ray was not observed in our γ-ray spectra, but its parent state is listed in Table IV. For every case of observed feeding we subtracted the measured yield of the feeding γ ray, i.e., Y_γ, from the total state yield Y_S. For every case of inferred feeding we subtracted the predicted yield of the feeding γ ray, i.e., $B \times Y_S'$, from the total state yield Y_S (where $Y_{S'}$ is the total state yield of the higher-lying state S' and B is the appropriate branching ratio to the interesting state). For example, in the case of the 1755 keV ^{32}P state (see Table IV), we observed feeding via the 1508 keV γ ray and inferred feeding via the 2658 keV ^{32}P state. To compute the 1755 keV direct state yield of $Y_S^S = (1.3 \pm 0.9) \times 10^{-3}$ we subtracted the observed 1508 keV γ-ray feeding of $Y_\gamma = (4.7 \pm 0.5) \times 10^{-3}$ and the inferred 2658 keV

state feeding of $B \times Y_S = 0.07 \times (7.3 \pm 0.8) \times 10^{-3}$ from the total state yield of $Y_S = (6.3 \pm 0.7) \times 10^{-3}$.

The resulting total and direct state yields from muon capture on ^{24}Mg, ^{28}Si, ^{31}P, and ^{32}S are listed in Table VI. These state yields are the weighted averages of the GeA and GeB data obtained from the isotopically enriched targets. The quoted errors include an overall normalization error of $\pm 10\%$, and the uncertainties from the γ-ray peak fitting and x-ray acceptance determinations. Also listed in Table VI are the ratios of the indirect and total state yields, i.e., the degree of feeding to the various levels. In a few cases, due to substantial feeding, the measurement uncertainties in the direct state yields are rather large.

E. Unidentified cascade feeding

A concern in determining the direct state yields is unidentified cascade feeding from higher lying states (i.e., feeding neither observed or inferred from the Ge singles data of Table IV). To test for unidentified cascade feeding, we determined for the interesting γ-ray lines the coincident γ-ray fraction (f_c) using both Ge singles data (method A) and Ge·CS coincidence data (method B). Unidentified cascade feeding was suggested if f_c extracted from the Ge·CS coincidence data (a measured sum of γ-ray coincidences) exceeded f_c from the Ge singles data (a computed sum of γ-ray coincidences). In addition, the measured energy spectrum of coincident γ rays (Ge·CS coincidence data) and predicted energy spectrum of coincident γ rays (Ge singles data) were analyzed for consistency. Due to signal-to-noise limitations, this analysis was performed on the natural isotopic abundance target data.

In method A we summed the yields of all coincident γ rays for each interesting γ ray using the data in Table IV. The summation included γ rays feeding directly or indirectly into the interesting photon's initial state and γ rays originating directly or indirectly from the interesting photon's final state. Dividing the summed yield of the coincident γ rays by the individual yield of the interesting γ ray gave f_c. In method B we measured the γ-ray coincidence fraction for each interesting γ ray using GeB·CSA coincidence data (we used GeB·CSA data rather than GeA·CSB data due to the

TABLE VI. Total state yields (Y_S), direct state yields (Y_S^S), and feeding fractions ($1-Y_S^S/Y_S$) for the (μ^-,ν) reaction on ^{24}Na, ^{28}Si, ^{31}P, and ^{32}S. The final states are labeled by the excitation energy (E_x) and spin parity (J^π). The dagger indicates unidentified cascade feeding of the relevant nuclear state is suspected and the double dagger indicates unidentified cascade feeding of the relevant nuclear state is untested (see text for details).

Final nucleus	E_x (keV)	J^π	Y_S ($\times10^{-3}$)	Y_S^S ($\times10^{-3}$)	$1-Y_S^S/Y_S$ (%)
^{24}Na	472	1^+	138 ± 16	$43.4\pm13.6^\ddagger$	69
^{24}Na	1341	2^+	42.4 ± 4.4	36.1 ± 4.3	15
^{24}Na	1347	1^+	43.7 ± 4.7	36.7 ± 4.6	16
^{24}Na	1846	2^+	7.0 ± 1.0	7.0 ± 1.0	0
^{24}Na	3372	2^-	7.7 ± 1.0	7.7 ± 1.0	0
^{24}Na	3413	1^+	7.2 ± 1.4	7.2 ± 1.4	0
^{28}Al	972	0^+	29.6 ± 3.6	5.5 ± 5.1	81
^{28}Al	1372	1^+	33.3 ± 6.1	$32.8\pm6.1^\dagger$	$2^\dagger$
^{28}Al	1620	1^+	16.4 ± 2.4	14.8 ± 2.4	10
^{28}Al	2138	2^+	49.0 ± 6.2	49.0 ± 6.2	0
^{28}Al	2201	1^+	76.8 ± 8.4	72.3 ± 8.5	6
^{28}Al	3105	1^+	16.9 ± 2.9	16.9 ± 2.9	0
^{28}Al	3876	2^-	10.6 ± 3.4	10.6 ± 3.4	0
^{31}Si	752	$1/2^+$	60.5 ± 6.7	1.8 ± 8.2	97
^{31}Si	1695	$5/2^+$	15.3 ± 1.6	$11.1\pm1.6^\dagger$	$27^\dagger$
^{31}Si	2317	$3/2^+$	9.9 ± 1.1	9.9 ± 1.1	10
^{31}Si	3133	$7/2^-$	2.6 ± 0.3	2.6 ± 0.3	0
^{31}Si	3534	$5/2^-$	25.6 ± 2.7	25.6 ± 2.7	0
^{31}Si	4383	$3/2^-$	3.5 ± 0.4	3.5 ± 0.4	0
^{31}Si	4720	$1/2^+$	26.7 ± 2.7	26.7 ± 2.7	0
^{31}Si	5282	$1/2^+$	10.1 ± 1.1	10.1 ± 1.1	0
^{32}P	1149	1^+	31.6 ± 3.2	20.8 ± 3.4	32
^{32}P	1323	2^+	19.5 ± 2.0	$16.1\pm2.4^\dagger$	$17^\dagger$
^{32}P	1755	3^-	6.6 ± 0.7	1.3 ± 0.4	80
^{32}P	2658	2^+	7.3 ± 0.8	7.3 ± 0.8	0
^{32}P	3264	2^-	23.2 ± 2.5	23.2 ± 2.5	0
^{32}P	3320	3^-	5.9 ± 0.6	5.9 ± 0.6	0
^{32}P	4205	1^+	25.8 ± 2.7	25.8 ± 2.7	0
^{32}P	4710	1^+	14.4 ± 1.5	14.4 ± 1.5	0

better energy resolution of the NaI CSA than the BGO CSB). We calibrated the CSA absolute photon acceptance using the 1.17 and 1.33 MeV coincident γ rays from ^{60}Co and corrected for the CSA acceptance energy dependence using the photon cross section tables of Ref. [23].

Four γ-ray lines from three nuclear levels yielded values of f_c via method B greater than values of f_c via method A, i.e., signalling unidentified cascade feeding. The states were the 1^+, 1372 keV level in ^{28}Al, the $5/2^+$, 1695 keV level in ^{31}Si, and the 2^+, 1323 keV level in ^{32}P. Their direct state yields (but *not* the corresponding γ-ray yields or total state yields) are identified as suspect in Table VI.

IV. RESULTS

In this section we discuss the partial capture rates for the (μ^-,ν) transitions obtained in this experiment for ^{24}Mg, ^{28}Si, ^{31}P, and ^{32}S and an earlier experiment for ^{23}Na [8]. We compare the results to earlier (μ,ν) data and shell model calculations. We also discuss the recent determinations of the effective coupling $\tilde{g}_p$ via muon capture on ^{23}Na and ^{28}Si.

Note the partial muon capture rates (Λ) are obtained by multiplying the tabulated direct state yields (Y_S^S) by the appropriate total muon capture rates [24].

A. The hyperfine effect in muonic ^{23}Na and ^{31}P

The observed transitions involve muon capture on both spin zero nuclei (^{24}Mg, ^{28}Si, and ^{32}S) and spin nonzero nuclei (^{23}Na and ^{31}P). In the latter case the muonic atom's $1S$ ground state is split into two hyperfine states $F_-=J_i-1/2$ and $F_+=J_i+1/2$,[1] and the observed capture rate Λ is a combination of the two hyperfine capture rates Λ_- and Λ_+. The exact combination of Λ_- and Λ_+ is determined by the initial ($t=0$) population of the F states, the μ-atom hyperfine transition rate Λ_h, the muon disappearance rate Λ_D, and the experimental time window for gamma-ray detection (i.e., the μSTOP gate). To compare measured and calculated rates, the relative population of the hyperfine states must be known.

The hyperfine effect in $\mu^-\ ^{23}$Na has been previously studied in Refs. [7] and [25]. In elemental sodium the measured hyperfine transition rate is $\Lambda_h=15.5\pm1.1\ \mu\mathrm{s}^{-1}$ [7] and the measured disappearance rate is $\Lambda_D=0.831\pm0.002\ \mu\mathrm{s}^{-1}$ [24]. Since $\Lambda_h\ll\Lambda_D$, the upper F_+ state rapidly empties into the lower F_- state, and the observed capture rate Λ is approximately the F_- capture rate Λ_-. Assuming the statistical population of the hyperfine states at $t=0$ [26], and accounting for the 2.0 μs μSTOP gate width in the ^{23}Na experiment [8], the observed capture rate is given by $\Lambda=0.97\Lambda_-+0.03\Lambda_+$.

For $\mu^-\ ^{31}$P, the circumstances surrounding the hyperfine effect are less certain. Direct investigations of the relative population of the F_+ and F_- states have been made by measurements of the μ-e asymmetry following muon decay in $\mu^-\ ^{31}$P. This method exploits the muon residual polarization, which is present in the $F_+=1$ state but absent in the $F_-=0$ state. Unfortunately, the two asymmetry experiments are in conflict, with Egorov *et al.* [27] obtaining $\Lambda_D\ll\Lambda_h$ and Lathrop *et al.* [28] obtaining $\Lambda_h\ll\Lambda_D$. The conventional theory of hyperfine transitions (i.e., $M1$ Auger emission), yields $\Lambda_h\ll\Lambda_D$ for muonic ^{31}P [29]. This is consistent with the data of Lathrop *et al.* [28] but inconsistent with the data of Egorov *et al.* [27]. In this paper we will assume $\Lambda_h\ll\Lambda_D$ and $\Lambda=\Lambda_-$ for muonic ^{31}P, as predicted in Ref. [29]. We note the preliminary results of a new measurement of hyperfine rate in muonic ^{31}P gives $\Lambda_h\sim50\ \mu\mathrm{s}^{-1}$ [30], i.e., $\Lambda\cong\Lambda_-$.

---

[1] For muonic ^{23}Na and muonic ^{31}P, the F_- hyperfine state is energetically lower than the F_+ hyperfine state, and hyperfine transitions increase the F_- state occupancy and decrease the F_+ state occupancy.

TABLE VII. Comparison of our γ-ray yields for muon capture on Mg and Si with the earlier results of Miller *et al.* and Pratt. The γ-ray yields are per muon capture *not* per muon stop, and include both direct and indirect production of the γ-ray parent state.

Final nucleus	γ-ray $E_i \rightarrow E_f$	This expt. $(\times 10^{-3})$	Miller *et al.* $(\times 10^{-3})$	Pratt $(\times 10^{-3})$
^{24}Na	$472 \rightarrow 0$	138 ± 16	167 ± 12	
^{24}Na	$1341 \rightarrow 472$	40.4 ± 4.2	36 ± 4	
^{24}Na	$1347 \rightarrow 472$	43.6 ± 4.7	40 ± 4	
^{24}Na	$1846 \rightarrow 1347$	2.8 ± 0.4		
^{24}Na	$1846 \rightarrow 472$		39 ± 4	
^{24}Na	$3372 \rightarrow 1347$	3.2 ± 0.4		
^{24}Na	$3413 \rightarrow 1341$	3.1 ± 0.6		
^{28}Al	$31 \rightarrow 0$		131 ± 13	
^{28}Al	$972 \rightarrow 31$	29.6 ± 3.6	20 ± 3	19 ± 9
^{28}Al	$1372 \rightarrow 31$	18.4 ± 3.4	17 ± 2	12 ± 17
^{28}Al	$1620 \rightarrow 31$	15.1 ± 2.2	17 ± 3	
^{28}Al	$1620 \rightarrow 0$		18 ± 3	
^{28}Al	$2138 \rightarrow 31$	19.4 ± 2.9		
^{28}Al	$2138 \rightarrow 0$	26.3 ± 3.8		
^{28}Al	$2201 \rightarrow 972$	10.6 ± 2.0	18 ± 3	
^{28}Al	$2201 \rightarrow 31$	62.6 ± 6.8	46 ± 3	
^{28}Al	$3105 \rightarrow 31$	12.7 ± 2.2		
^{28}Al	$3876 \rightarrow 0$	8.4 ± 2.7		
^{28}Al	$7725 \rightarrow 0$		54 ± 40	

B. Comparison to earlier (μ^-, ν) yield data

Earlier measurements of gamma-ray yields and state yields have been published by Miller *et al.* [31] for ^{24}Mg and ^{28}Si (using enriched ^{24}MgO and ^{28}SiO$_2$ targets) and by Pratt [32] for Si and S (using natural isotopic abundance Si and S targets). Table VII compares our results for γ-ray yields on ^{24}Mg and ^{28}Si to the earlier studies. Table VIII compares our results for state yields on ^{32}S to the earlier studies. In our experiment we have identified additional γ rays and states,

TABLE VIII. Comparison of our total state yields for muon capture on S with the earlier results of Pratt. The total state yields are per muon capture *not* per muon stop, and include both direct and indirect production of the parent state.

Final nucleus	State E_x	This expt. $(\times 10^{-3})$	Pratt expt. $(\times 10^{-3})$
^{32}P	1149	31.6 ± 3.2	18 ± 4
^{32}P	1323	19.5 ± 2.0	17 ± 5
^{32}P	1755	6.6 ± 0.7	27 ± 29
^{32}P	2658	7.3 ± 0.8	
^{32}P	3264	23.2 ± 2.4	35 ± 15
^{32}P	3320	5.9 ± 0.6	
^{32}P	4036		16 ± 14
^{32}P	4205	25.8 ± 2.7	
^{32}P	4663		16 ± 6
^{32}P	4710	14.4 ± 1.5	
^{32}P	4876		2.9 ± 2.3

and resolved several discrepancies between earlier γ-ray yield data and accepted γ-decay branching ratios.

For $\mu^- $Mg, Table VII lists Miller's results for four ^{24}Na γ-ray transitions and our results for six ^{24}Na γ-ray transitions. For the three transitions $472 \rightarrow 0$, $1341 \rightarrow 472$, and $1347 \rightarrow 472$ Miller's yield data and our yield data are in reasonable agreement. However, for the 1846 keV state, Miller's γ-ray yield for the $1846 \rightarrow 472$ transition ($B = 0.25$) of $(39 \pm 4) \times 10^{-3}$ and our γ-ray yield for the $1846 \rightarrow 1347$ transition ($B = 0.40$) of $(2.8 \pm 0.4) \times 10^{-3}$, are obviously inconsistent. We suspect, in Miller's data, the interesting $1846 \rightarrow 472$ ^{24}Na line is contaminated by the strong $1368 \rightarrow 0$ ^{24}Mg background line (i.e., Miller's $1846 \rightarrow 472$ is mainly $1368 \rightarrow 0$). If Miller's yield of the $1846 \rightarrow 472$ ^{24}Na line were correct, our yield of the $1846 \rightarrow 1374$ ^{24}Na line would be 20 times larger than we observed (based upon the accepted branching ratios of 0.25 and 0.40, respectively).

For $\mu^- $Si, Table VII lists Miller's results for seven ^{28}Al γ-ray transitions and our results for nine ^{28}Al γ-ray transitions. While Miller's data and our data are in general agreement, there are some inconsistences. Firstly, for the $2201 \rightarrow 31$ and $2201 \rightarrow 972$ transitions, Miller's yields of $(46 \pm 3) \times 10^{-3}$ and $(18 \pm 3) \times 10^{-3}$, and our yields of $(62.6 \pm 6.8) \times 10^{-3}$ and $(10.6 \pm 2.0) \times 10^{-3}$, are significantly different. In favor of our results, the accepted branching ratios of 0.79 and 0.16 for the $2201 \rightarrow 31$ and $2201 \rightarrow 972$ transitions [22] are consistent with our yield data but inconsistent with Miller's yield data. Secondly, while Miller *et al.* report similar γ-ray yields for the $1620 \rightarrow 31$ and $1620 \rightarrow 0$ transitions, we see the former but not the latter. In favor of our results, the accepted branching ratios of 0.92 and 0.06 for the $1620 \rightarrow 31$ and $1620 \rightarrow 0$ transitions [22] are consistent with our yield data but inconsistent with Miller's yield data.

For $\mu^- $ ^{28}Si we also report yields for several weaker transitions not observed by Miller *et al.*, while Miller *et al.* report yields for two transitions either below (the $31 \rightarrow 0$ transition) or above (the $7725 \rightarrow 0$ transition) our energy window for photon detection. Lastly, also listed in Table VII are γ-ray yields, for the transitions $972 \rightarrow 31$ and $1372 \rightarrow 0$, from Pratt [32]. Pratt's γ-ray yields are consistent with our results and Miller's results, but the experimental uncertainties are large.

For $\mu^- $ ^{32}S, Table VIII lists Pratt's results and our results for total state yields (Y_S) to various states in ^{32}P (note Pratt's data are for a natural S target and our data are for an enriched ^{32}S target). For states observed in both Pratt's data and our data the various yields are generally consistent (the experimental uncertainties in Pratt's data are quite large). However, an exception is the 1149 keV level where our yield is $(31.6 \pm 3.2) \times 10^{-3}$ and Pratt's yield is $(18 \pm 4) \times 10^{-3}$. In our case, we observed three γ-ray lines from the 1149 keV parent state, and their relative intensities were in accord with the accepted branching ratios of [22]. In Pratt's case, unfortunately no information for the observed γ-ray lines and the corresponding γ-ray yields was given. Lastly, we report yields for four states at higher energies not seen by Pratt (at 2658, 3320, 4205, and 4710 keV), but do not confirm pro-

duction of three states (at 4036, 4663, and 4876 keV) seen by Pratt at the 1–2 σ level of statistical significance.

C. Comparison to the 1s-0d shell model

In this section we report the results of shell model calculations for the observed allowed GT transitions from muonic ^{23}Na, ^{24}Mg, ^{28}Si, ^{31}P, and ^{32}S (the ^{23}Na results were reported previously in Ref. [8]). We compare measured and calculated rates, extract a ''best fit'' value of the effective weak axial coupling $\tilde{g}_a$, and discuss the sum and distribution of Gamow-Teller transitions in muon capture. Lastly, we compare our muon capture studies to earlier β-decay studies.

Comprehensive formulas for nuclear muon capture rates have been published by Morita and Fujii in Ref. [33] and by Walecka in Ref. [34]. In computing the capture rates we employed the impulse approximation, considering the weak nuclear current as the sum of Z one-body weak nucleonic currents. Specifically, as described by Brown and Wildenthal in Ref. [35], the required nuclear matrix elements were expressed as sums of products of one-body transition densities (OBTDs) and single particle matrix elements (SPMEs). In this scheme the nuclear model dependences are contained in the OBTDs and the weak coupling constant dependences are contained in the SPMEs.

The OBTDs were calculated with the OXBASH shell model computer code [36] using the full $1s$-$0d$ space and the universal SD interaction. Brown and Wildenthal [37] obtained the $0d_{5/2}$, $1s_{1/2}$, and $0d_{3/2}$ single particle energies and the 64 A-dependent two-body matrix elements of the universal SD interaction from a least squares fit to 440 energy levels of $1s$-$0d$ shell nuclei. The universal SD interaction has been extensively tested for various observables in the $A=17$–39 region.

The SPMEs were calculated assuming harmonic oscillator nuclear wave functions and taking $\hbar\omega = 45/A^{1/3} - 25/A^{2/3}$. The momentum transfer was determined according to energy-momentum conservation via

$$\nu + \nu^2/2M_i = m_\mu - (E_f - E_i) - \epsilon_b, \qquad (6)$$

where ν is the neutrino three-momentum, m_μ and M_i are the muon and target masses, and E_i, E_f and ϵ_b are the initial nuclear state, final nuclear state, and μ-atom binding energies. The coupling constants of the nucleon's weak interaction are the vector (g_v), weak magnetic (g_m), and scalar (g_s) couplings of the polar vector weak current, and the axial (g_a), induced pseudoscalar (g_p), and tensor (g_t) couplings of the axial vector weak current. For the capture rates of the allowed GT transitions in Table VI, the weak axial coupling g_a generally dominates the other weak couplings. In our capture rate calculations the effective value of the axial coupling was obtained by a least-squares fit of the calculated rates to the measured rates (the coupling constant renormalization encompassing effects such as the model space truncation and two-body exchange currents that are omitted in our calculation). For the couplings g_v, g_m, g_s, and g_t, we have assumed $g_v = 1.0$ and $g_m = 3.706$ as predicted by the conserved vector current hypothesis (CVC) [38,39], and $g_s = g_t = 0$ as

predicted by G-parity conservation [40]. For the induced pseudoscalar coupling we used $g_p = -7$ as predicted by the partially conserved axial current hypothesis (PCAC) [1], and $g_p = 0$ and $g_p = -15$ to test the coupling sensitivity of the capture rates.

Lastly, to compute the rates, we assumed a constant value for the muon wave function in the nuclear interior, i.e., $\phi_{1S}(r) \rightarrow \phi_{1S}(0)$. By numerically solving the Dirac equation, a number of authors [41,42] have computed the values of $\phi_{1S}(0)$ for an extended nuclear charge distribution. The difference between a pointlike and finite nuclear charge distribution is generally parametrized by either an effective nuclear charge Z_{eff} or a wave-function reduction factor R. We interpolated the values for R of Ref. [42] to our target nuclei ^{23}Na, ^{24}Mg, ^{28}Si, ^{31}P, and ^{32}S.

For the $1s$-$0d$ shell nuclei ^{23}Na, ^{24}Mg, ^{28}Si, ^{31}P, and ^{32}S, there are typically 10–15 states of excitation energies $\leqslant 6000$ keV with J^π assignments corresponding to allowed GT transitions. The shell model, however, usually predicts the vast majority of GT strength to be concentrated into a small fraction of the possible transitions. The dominant transitions in our shell model calculation are to levels at 1017, 1823, 3432, and 3458 keV in ^{23}Ne, 1347 and 3413 keV in ^{24}Na, 1372, 2201, 3105, and 4846 keV in ^{28}Al, 752, 4259, and 4720 keV in ^{31}Si, and 1149, 4205, and 4710 keV in ^{32}P (the identification of the model states with the experimental states was not problematic). Of these 16 transitions, 14 are clearly observed and two are possibly observed in our (μ,ν) data. The latter two cases are the 4259 keV ^{31}Si transition and the 4846 keV ^{28}Al transition discussed in detail in Sec. III B. We conclude that we find a near one-to-one correspondence between the predicted strong GT transitions and the experimentally observed GT transitions (i.e., good qualitative agreement between the model and the data).

A comparison of the calculated and measured capture rates is given in Table IX and Fig. 2 (we present both the individual GT capture rates and the per-target summed GT capture rates). Several GT transitions with state yields listed in Table VI are omitted from the comparisons in Table IX and Fig. 2. Firstly, we have omitted the allowed GT transitions to the 472 keV state in ^{24}Na, the 1372 keV state in ^{28}Al, and the 752 keV state in ^{31}Si. In each of these cases, the contribution of cascade feeding to the total state yield is either large or uncertain, and their direct state yields were therefore deemed untrustworthy (for details see Sec. III E). In addition, the ^{23}Na$(3/2^+,0) \rightarrow {}^{23}Ne(5/2^+,2315)$ transition and the ^{31}P$(1/2^+,0) \rightarrow {}^{31}Si(3/2^+,2317)$ were omitted from Table IX and Fig. 2. Both are $\Delta J = J_f - J_i = +1$ transitions from the F_- hyperfine states of $J_i \neq 0$ spin nuclei. For these special cases, the arguments for the dominance of the product of the axial coupling constant and the $J_0(\nu r)\sigma\tau^\pm$ matrix element are not valid (see for example Ref. [14,34]). Therefore, because of the special features of these particular transitions, they were omitted.

The ''best fit'' value of the effective weak axial coupling, from the least-squares fit of the allowed GT transitions in Table IX and Fig. 2, is $\tilde{g}_a = -0.91^{+0.13}_{-0.16}$ using $g_p = -7.0$. Using $\tilde{g}_p = 0$ and $\tilde{g}_p = -15$ we obtained $\tilde{g}_a = -0.83^{+0.13}_{-0.15}$ and

TABLE IX. Measured and calculated rates for the observed Gamow-Teller transitions from muon capture on ^{23}Na, ^{24}Mg, ^{28}Si, ^{31}P, and ^{32}S. For the calculation we used $g_a = -0.91$ and $g_p = -7.0$.

Final nucleus	Excitation energy (keV)	J^π	Λ^{exp} ($\times 10^3$ s^{-1})	Λ^{th} ($\times 10^3$ s^{-1})
^{23}Ne	1017	$1/2^+$	4.9 ± 1.4	4.4
^{23}Ne	1823	$3/2^+$	4.1 ± 0.9	5.2
^{23}Ne	3432	$3/2^+$	4.1 ± 0.8	2.0
^{23}Ne	3458	$1/2^+$	10.4 ± 2.2	7.5
^{23}Ne sum			23.5	19.1
^{24}Na	1347	1^+	17.5 ± 2.3	18.9
^{24}Na	3413	1^+	3.5 ± 0.7	7.5
^{24}Na sum			21.0	26.4
^{28}Al	1620	1^+	12.9 ± 2.1	2.1
^{28}Al	2201	1^+	62.8 ± 7.4	22.4
^{28}Al	3105	1^+	14.7 ± 2.6	16.2
^{28}Al sum			90.4	40.7
^{31}Si	4720	$1/2^+$	31.6 ± 3.2	42.2
^{31}Si	5282	$1/2^+$	12.0 ± 1.3	0.24
^{31}Si sum			43.6	42.4
^{32}P	1149	1^+	28.1 ± 4.5	14.9
^{32}P	4205	1^+	34.8 ± 3.6	23.9
^{32}P	4710	1^+	19.4 ± 2.1	36.9
^{32}P sum			82.3	75.7

$g_a = -0.96^{+0.14}_{-0.15}$, respectively, i.e., indicating minor changes in the coupling $\tilde{g}_a$ for quite substantial changes in the coupling $\tilde{g}_p$. Including the GT transitions to the 472 keV state in ^{24}Na, 1372 keV state in ^{28}Al, and 752 keV state in ^{31}P (where cascade feeding is troublesome) yielded $g_a = -0.97^{+0.13}_{-0.16}$, i.e., little effect on the ''best fit'' value of the axial coupling. Note that, in the fitting of the calculated rates to the measured rates, because the model uncertainties are generally greater than the experimental uncertainties, we did not simply weight the data points by the experimental errors. Rather, the points were weighted by the addition in quadrature of the individual experimental uncertainties and a global theoretical uncertainty. The global theoretical uncertainty was determined by requiring the χ^2_{pdf} of the fit to be one. In this manner, the quoted errors in the effective axial coupling $\tilde{g}_a$ include both experimental and model uncertainties (the experimental errors include the uncertainties in the peak fitting, acceptance determination, and the overall normalization error of $\pm 10\%$).

As mentioned above, the best fit value of $\tilde{g}_a = -0.91^{+0.13}_{-0.16}$ was extracted assuming $\tilde{g}_p = -7.0$. Using the variation in the best fit values of the effective axial coupling for $\tilde{g}_p = 0$, -7, and -15 we have computed an additional uncertainty in $\tilde{g}_a$ of $^{+0.08}_{-0.05}$ from the present knowledge of $\tilde{g}_p$. Adding the uncertainties of $^{+0.13}_{-0.16}$ and $^{+0.08}_{-0.05}$ in quadrature, we get a final value for the effective axial coupling of $\tilde{g}_a = -0.91^{+0.15}_{-0.17}$ which includes the uncertainties in the experiment, model, and the induced pseudoscalar coupling constant.

Examining the capture rates for individual transitions,

Table IX and Fig. 2 show that, although there is a definite correlation between the measured rates and calculated rates, the model–data discrepancies are numerous and substantial. For example, for the transition to the 1620 keV ^{28}Al state the model predicts 2.1×10^3 s^{-1} whereas the data yields $(12.9 \pm 2.1) \times 10^3$ s^{-1}, and for the transition to the 3413 keV ^{24}Na state the model predicts 7.5×10^3 s^{-1} whereas the data yields $(3.5 \pm 0.7) \times 10^3$ s^{-1} (i.e., there are examples of the model substantially over- and under-predicting the measured values). Of the 14 GT transitions in Table IX and Fig. 2, only five cases have their calculated rates and measured rates within 2 σ (expt).

Examining the per-target summed capture rates, Table IX and Fig. 2 show experiment and theory in significantly better agreement. By far the most obvious discrepancy is the summed capture rate for ^{28}Si where the model gives 41×10^3 s^{-1} and the data gives 90×10^3 s^{-1}. Overall it seems that while the model performs a fair job for the per-target summed GT transition rates, it performs a poor job for the individual GT transition rates.

It is instructive to compare our results for allowed GT muon capture with Brown and Wildenthal's results for allowed GT β decay [35]. Firstly, the ''best fit'' values of $\tilde{g}_a$ from our muon capture work and their β-decay work are entirely consistent, $g_a = -0.91^{+0.15}_{-0.17}$ and $g_a = -0.95 \pm 0.04$ [35], respectively (note these effective values of the coupling $\tilde{g}_a$ are considerably smaller than the free nucleon value $g_a = -1.266 \pm 0.004$ [43]). Secondly, both the muon capture results and the β-decay results indicate better agreement between the model and the data for the per-target summed rates than the individual transition rates (i.e., the calculation is better at reproducing the sum of the GT transitions than the fragmentation of the GT transitions). However, for both the summed rates and the individual rates, the agreement of experiment and theory is better in the β-decay case than the muon capture case.

Why is the agreement between theory and experiment better for β decay than μ capture? In β decay the momentum transfer–squared is $q^2 \simeq 0$ whereas in muon capture the momentum transfer–squared is $q^2 \simeq -0.9 \, m^2_\mu$. Most likely this q^2 difference is the root cause of the greater disagreement of experiment and theory for allowed GT transitions in μ capture compared to β decay. Firstly, the dominant operator for allowed GT transitions, in muon capture and β decay, is $J_0(\nu r)\sigma\tau^\pm$. In the case of β decay, where $q^2 \simeq 0$, the spherical Bessel function $J_0(\nu r)$ is essentially constant over the nuclear volume, and the matrix element of $J_0(\nu r)\sigma\tau^\pm$ is insensitive to the radial form of the nuclear wave functions. However, in the case of muon capture, where $q^2 \simeq -0.9 \, m^2_\mu$, the spherical Bessel function $J_0(\nu r)$ varies significantly over the nuclear volume, and the matrix element of $J_0(\nu r)\sigma\tau^\pm$ is sensitive to the radial form of the nuclear wave functions. This results in an additional source of model uncertainty, present in muon capture but absent in β decay. Secondly, the role of operators other than $J_0(\nu r)\sigma\tau^\pm$ is of order q/M [in the $q^2 \to 0$ limit only the operator $J_0(\nu r)\sigma\tau^\pm$ contributes]. Consequently, although in β decay such operators are negligible, they are significant in muon capture. This

also results in an additional source of model uncertainty, present in muon capture but absent in β decay.

Lastly, calculations of muon capture rates, using the full $1s$-$0d$ space and universal SD interaction, were recently reported by Siiskonen *et al.* The partial muon capture rates obtained by us and Ref. [44] are in good agreement. However, in the case of nonzero spin nuclei, Siiskonen *et al.* calculate the statistically averaged muon capture rates only (i.e., not the individual capture rates from the two hyperfine states). In the case of ^{23}Na, where capture is from a nonstatistical mixture of hyperfine states [8], the comparison of the calculated statistical capture rate with the measured nonstatistical capture rate, as made in Ref. [44], is inappropriate.

D. Utilization of measured GT transition probabilities

The (p,n) and (n,p) charge exchange (CEX) reactions, at medium energies and forward angles, are established probes of Gamow-Teller excitations in nuclei [45–47]. Their use to map the quenching of GT strength is a milestone topic in nuclear physics. In addition, the derived GT transition probabilities for selected GT transitions have been key elements for the understanding of supernova dynamics, neutrino detection, and double β decay.

Measurements of both (p,n) and (n,p) reactions have been made for many $1s$-$0d$ shell nuclei. In the case of the allowed GT transitions in Table IX, corresponding (n,p) CEX data are available for the transitions in ^{23}Na (Siebels *et al.* [48]) and ^{31}P (Sedlar *et al.* [50]), and corresponding (p,n) CEX data are available for the transitions in ^{24}Mg, ^{28}Si, and ^{32}S (Anderson *et al.* [49,51]). In the former case identical transitions are probed in the (n,p) and (μ^-,ν) data, in the latter case analog transitions are probed in the (p,n) and CEX data. In this section we compare (μ^-,ν) capture rates calculated using shell model values of the $\sigma\tau^{\pm}$ matrix elements (calc. A) with (μ^-,ν) capture rates calculated using CEX reaction values of the $\sigma\tau^{\pm}$ matrix elements (calc. B). The results might illuminate the sources of the aforementioned discrepancies between the measured and calculated (μ^-,ν) capture rates of Sec. IV C.

Muon capture rates for allowed GT transitions may be written in the form

$$\Lambda = f(\alpha[101]^2 + \beta[101] + \gamma). \tag{7}$$

In Eq. (7) f is a phase space factor, [101] is the matrix element of the operator $J_0(\nu r)\sigma\tau^{\pm}$ (in the notation of Morita [33]), the term α is a combination of the weak coupling constants, the term β is a combination of the weak coupling constants and contributing matrix elements not including [101], and the term γ is a combination of the weak coupling constants and matrix elements products not including [101]. Generally, for allowed GT transitions, the first term (i.e., $\alpha[101]^2$) dominates.

The matrix element of the operator $J_0(\nu r)\sigma\tau^{\pm}$ can be decomposed into two components; the matrix element of the spin-isospin operator $\sigma\tau^{\pm}$ (acting on spin-isospin coordinates only) and the matrix element of the spherical Bessel function $J_0(\nu r)$ (acting on spatial coordinates only). To in-
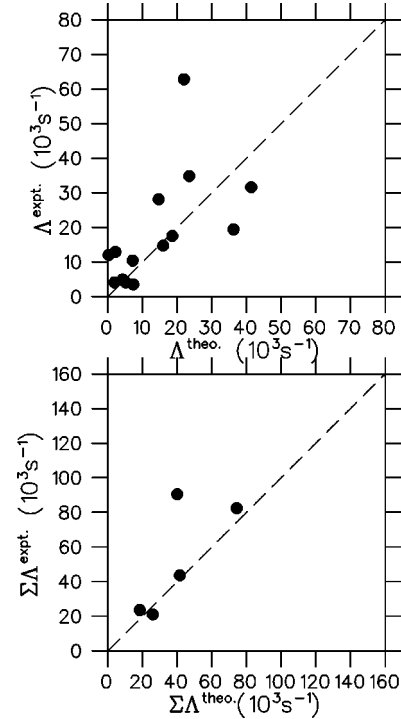

FIG. 2. Measured versus calculated rates for the allowed Gamow-Teller transitions from muon capture on ^{23}Na, ^{24}Mg, ^{28}Si, ^{31}P, and ^{32}S. The upper plot shows the individual capture rates and the lower plot shows the per-target summed capture rates.

corporate the $(p,n)/(n,p)$ charge exchange data into the (μ^-,ν) capture rate calculations we have replaced the shell model values for the matrix elements of $\sigma\tau^{\pm}$ (calc. A) with the CEX reaction values for the matrix elements of $\sigma\tau^{\pm}$ (calc. B). Note, we continue to employ the shell model in computing the other contributing matrix elements [i.e., the matrix element of $J_0(\nu r)$ and the matrix elements in β and γ of Eq. (7)]. Also note, we use $g_a = -1.26$ (the free nucleon value) in calc. B but $g_a = -0.91$ (the effective nucleon value) in calc. A. In calc. B (unlike calc. A), the quenching of GT strength is included in the experimentally determined $\sigma\tau^{\pm}$ matrix elements and not via an effective axial coupling constant.

The (μ^-,ν) capture rates obtained from calc. A and calc. B are listed in Table X and plotted in Fig. 3. In Table X and Fig. 3, as in Sec. IV C, we have omitted the 472 keV ^{24}Na, 1372 keV ^{28}Al, and 752 keV ^{31}Si transitions (due to cascade feeding), and the 2315 keV, ^{23}Ne and 2317 keV, ^{31}Si transitions (due to the special features of F_- capture rates for $J_i \rightarrow J_i + 1$ transitions). Also, for the 3432 and 3458 keV transitions in ^{23}Ne we quote only a summed rate as these transitions are not resolved in the ^{23}Na(n,p) data [48]. Lastly, the 4720 and 5282 keV transitions in ^{31}Si are omitted as these transitions are not resolved from other possible allowed transitions in the ^{31}P data [50].

Comparison of the calc. A and calc. B results show a significant improvement in the overall agreement of the measured and calculated (μ^-,ν) capture rates when the CEX reaction $\sigma\tau^{\pm}$ matrix elements, rather than the shell model $\sigma\tau^{\pm}$ matrix elements, are used (the χ^2 between experiment

TABLE X. Results of muon capture rate calculations using shell model values (calc. A) and $(p.n)/(n,p)$ charge exchange values (calc. B) for the Gamow-Teller ($\sigma\tau^{\pm}$) matrix elements. In calc. A we have used $g_a = -0.91$ and in calc. B we have used $g_a = -1.26$ (see text for details). For the transitions to the 3432 keV, $3/2^+$ and 3458 kev, $1/2^+$ states in ^{23}Ne we quote a summed capture rate only.

Final nucleus	Excitation energy (keV)	J^{π}	Λ^{exp} ($\times 10^3$ s^{-1})	Λ^{th} (calc. A) ($\times 10^3$ s^{-1})	Λ^{th} (calc. B) ($\times 10^3$ s^{-1})
^{23}Ne	1017	$1/2^+$	4.9 ± 1.4	4.4	3.5
^{23}Ne	1823	$3/2^+$	4.1 ± 0.9	5.2	4.3
^{23}Ne	3400	$3/2^+, 1/2^+$	14.5 ± 0.8	9.5	16.6
^{24}Na	1347	1^+	17.5 ± 2.3	18.9	20.8
^{24}Na	3413	1^+	3.5 ± 0.7	7.5	9.2
^{28}Al	1620	1^+	12.9 ± 2.1	2.1	4.8
^{28}Al	2201	1^+	62.8 ± 7.4	22.4	45.6
^{28}Al	3105	1^+	14.7 ± 2.6	16.2	6.7
^{32}P	1149	1^+	28.1 ± 4.5	14.9	19.8
^{32}P	4205	1^+	34.8 ± 3.6	23.9	55.3
^{32}P	4710	1^+	19.4 ± 2.1	36.9	18.7

and calculation is 21.7 for calc. A and 11.6 for calc. B). For example, (i) the 2201 keV ^{28}Al transition, with a measured capture rate of 62.8×10^3 s^{-1}, has corresponding calculated rates of 22.4×10^3 s^{-1} (calc. A) and 45.6×10^3 s^{-1} (calc. B) and (ii) the 4710 keV ^{32}P transition, with a measured capture rate of 19.4×10^3 s^{-1}, has corresponding calculated rates of
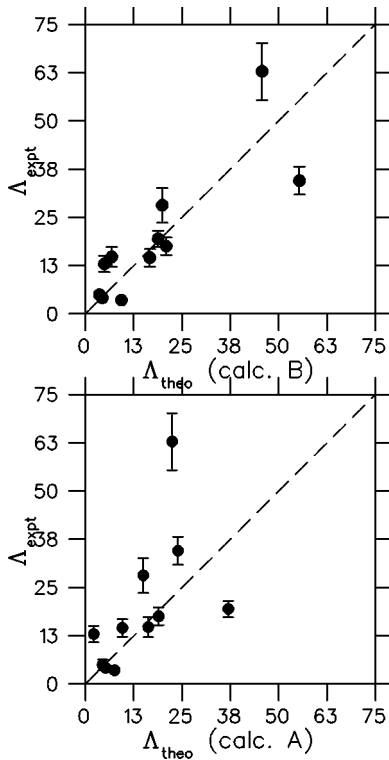

FIG. 3. Results of muon capture rate calculations using shell model values (calc. A) and $(p.n)/(n,p)$ charge exchange values (calc. B) for the Gamow-Teller $\sigma\tau^{\pm}$ matrix elements. In calc. A we have used $g_a = -0.91$ and in calc. B we have used $g_a = -1.26$ (see text for details). For the transitions to the 3432 keV, $3/2^+$ and 3458 keV, $1/2^+$ states in ^{23}Ne we quote a summed capture rate only.

36.9×10^3 s^{-1} (calc. A) and 18.8×10^3 s^{-1} (calc. B). Especially noteworthy is the fragmentation of GT strength in ^{28}Si, which is reproduced much better with the CEX reaction values than the shell model values of the $\sigma\tau^{\pm}$ matrix elements. However, the improved agreement of calc. B compared to calc. A is not universal. The 4200 keV ^{32}P transition, with a measured capture rate of 34.5×10^3 s^{-1}, has corresponding calculated rates of 28.2×10^3 s^{-1} (calc. A) and 55.3×10^3 s^{-1} (calc. B).

The significant overall improvement in the model-data agreement for calc. B compared to calc. A indicates inaccuracies in the shell model GT matrix elements are a partial source of the discrepancies between the data and calc. A. That some discrepancies between calc. B and the data exist, is consistent with shell model inaccuracies in the $J_0(\nu r)$ radial matrix element and the $O(q/M)$ matrix elements (see Sec. IV C).

E. Comments on determinations of g_p in nuclear muon capture

As discussed earlier, from recent measurements of hyperfine dependences in muon capture on ^{23}Na and angular correlations in muon capture on ^{28}Si, effective values for the induced pseudoscalar coupling have been determined. The results, $\tilde{g}_p = (6.5 \pm 2.4)\tilde{g}_a$ for ^{23}Na [8] and either $\tilde{g}_p = (0 \pm 3.2)\tilde{g}_a$ [11] or $\tilde{g}_p = (-3 \pm 1.5)\tilde{g}_a$ [10] for ^{28}Si, are inconsistent. Note, the capture rates themselves, as discussed in Sec. IV C, are generally insensitive to $\tilde{g}_p$.

One possible source for the conflicting results is the model sensitivity of the extracted coupling, i.e., inaccuracies in the calculation of the necessary nuclear matrix elements for either ^{23}Na, ^{28}Si, or both. In the Fujii-Primakoff approximation (for example see Ref. [14]) $O(q/M)$ nuclear matrix elements [i.e., matrix elements other than $J_0(\nu r)\sigma\tau^{\pm}$] are ignored, and the hyperfine dependences and angular correlations in allowed GT transitions are nuclear model independent. However, in realistic model calculations [8,12,44]

$O(q/M)$ matrix elements are not negligible, and the hyperfine dependences and angular correlations show significant model dependences. The corresponding capture rates themselves, which are generally dominated by the effective axial coupling and the $J_0(\nu r)\sigma\tau^{\pm}$ matrix element, offer clear-cut tests of the quality of the model.

In the case of ^{28}Si, the measured and calculated muon capture rates for the observed GT transitions (see Table IX) shows substantial discrepancies. Specifically, for the transitions to the 1620 and 2201 keV states, the measured capture rates of $(12.9\pm2.1)\times10^3\,\mathrm{s}^{-1}$ and $(62.8\pm7.4)\times10^3\,\mathrm{s}^{-1}$ are much greater than the calculated capture rates of $2.1\times10^3\,\mathrm{s}^{-1}$ and $22.4\times10^3\,\mathrm{s}^{-1}$. It appears, in muon capture on ^{28}Si, the shell model does a poor job for the observed distribution of the Gamow-Teller strength. Especially worrisome is the 2201 keV transition, where the effective value of the coupling $\tilde{g}_p$ is obtained by reproducing the measured angular correlations, when the standard value of the effective axial coupling ($\tilde{g}_a\simeq-1$) is unable to reproduce the measured capture rate. Trusting the former result, given the latter result, is probably unjustified.

In the case of ^{23}Na, the measured and calculated muon capture rates for the observed GT transitions (see Table IX) show better agreement. The largest discrepancy is for the transition to the 3432 keV $1/2^+$ state, where the data yields $(4.1\pm0.8)\times10^3\,\mathrm{s}^{-1}$ and the model yields $2.0\times10^3\,\mathrm{s}^{-1}$. For the other transitions, the model and data are within the experimental uncertainties. In the ^{23}Na hyperfine dependence analysis, the effective coupling $\tilde{g}_p$ was obtained by a least squares fit of the hyperfine dependences of all observed GT transitions. The better agreement of the measured and calculated capture rates for ^{23}Na compared to ^{28}Si, probably favors the effective value of $\tilde{g}_p$ from ^{23}Na over ^{28}Si.

Last, we stress that while better agreement between measured and calculated rates is a reason to favor the ^{23}Na value for $\tilde{g}_p$ over the ^{28}Si value for $\tilde{g}_p$, $O(q/M)$ nuclear matrix elements, contributing to the hyperfine dependences and angular correlations, are poorly tested by the capture rate data. We strongly encourage more extensive investigations of the model dependences of the extracted values of $\tilde{g}_p$ for ^{23}Na and ^{28}Si. We note the interesting recent study of effective operators for muon capture on ^{28}Si by Siiskonen, Suhonen, and Hjorth-Jensen [52].

V. SUMMARY

In conclusion, using a pair of Compton-suppressed Ge detectors and the TRIUMF M9B decay-muon beamline, we have measured yields for 38 γ-ray lines and 29 (μ^-,ν) transitions following muon capture on ^{24}Mg, ^{28}Si, ^{31}P, and ^{32}S. Our results, supplemented with previous data on ^{23}Na [8], yield an extensive body of capture rate data across the $1s$-$0d$ shell. Additionally, our results resolve several inconsistences of previously measured γ-ray yields and accepted γ-decay branching ratios.

For the allowed Gamow-Teller transitions, we have compared measured and calculated capture rates. The capture rate calculations were performed with the OXBASH computer code, the full $1s$-$0d$ space, and the universal SD interaction.

We found a ''best fit'' value of the effective axial coupling of $\tilde{g}_a=-0.91^{+0.15}_{-0.17}$. We observed fair agreement between model and data for the per-target summed GT capture rates, but poor agreement between model and data for the individual GT capture rates. Our value of $\tilde{g}_a$, and our observation of better agreement for summed rates than individual rates, is consistent with studies of allowed GT transitions in nuclear β decay. However, the model versus data agreement is clearly poorer for muon capture than for β decay.

We have also calculated muon capture rates with the shell model $\sigma\tau^{\pm}$ matrix element values (calc. A) replaced by values from (n,p) and (p,n) reaction data (calc. B). We found the latter calculations (calc. B) give significantly improved agreement with the muon capture data compared to the former calculations (calc. A).

Lastly, we have discussed the conflicting values of $\tilde{g}_p$ extracted from recent measurements of hyperfine dependences in muon capture on ^{23}Na and angular correlations in muon capture on ^{28}Si. We point out that the capture rates are well defined tests of the model calculations of the $\sigma\tau^{\pm}$ matrix elements. The better agreement of the measured and calculated capture rates for ^{23}Na compared to ^{28}Si, is a reason to favor the ^{23}Na result over the ^{28}Si result. However, we urge more detailed studies of the role of the $O(q/M)$ matrix elements and the model dependences of the extracted values of the coupling $\tilde{g}_p$ in ^{23}Na and ^{28}Si.

APPENDIX: CORRECTION FACTORS TO THE Ge DETECTOR ACCEPTANCES

Several minor corrections were applied in the calculation of the Ge detector acceptances and the γ-ray yields. The corresponding correction factors C_{bm}, C_{lt}, C_{ab}, and C_{sv} are described below.

The correction factor C_{bm} is related to muon stops not identified by the beam telescope (caused by a sagging gain in the S1 photomultiplier for a portion of the experiment). At very low μ^- fluxes, when a muon stop is not identified the μSTOP gate is not opened and μ^- capture γ rays are not recorded (making a correction unnecessary). At higher μ^- fluxes, however, a γ ray from an unidentified muon stop may randomly fall in the μSTOP gate of an identified muon stop (making a correction necessary). To determine the correction factor C_{bm} we measured the beam telescope inefficiency on a run-by-run basis by comparing the number of observed muonic x rays with and without an accompanying S1·S2·$\overline{\text{S1}}$ pulse. From the beam telescope inefficiency (η), the muon stop rate (ϕ_μ), and the μSTOP gate width (t_μ), we then computed the correction C_{bm} (it is approximately $\eta\phi_\mu t_\mu$). The resulting values of the correction factor C_{bm} ranged from 0.95 to 1.00.

The correction factor C_{lt} is related the 2.0 μs width of the μSTOP gate in the trigger logic. The 2.0 μs μSTOP gate width was chosen as a compromise between maximizing the muon capture γ rays, and minimizing the background γ rays, recorded. However, due to the 1.067, 0.756, 0.611, and 0.555 μs lifetimes of the Mg, Si, P, and S muonic atoms [24] a small fraction of γ rays fall outside their μSTOP gate. Ignoring muon pileup effects, the correction factor for this gating effect is $C_{lt} = 1 - \exp(t_w/\tau)$ where t_μ is the μSTOP gate width and τ is the muonic atom lifetime. Values of the correction factors C_{lt}, including muon pileup effects, ranged from 0.96 to 0.98. Note this correction factor applies only to the delayed γ-rays [and Eq. (4)] and not the prompt x rays [and Eq. (1)].

The correction factor C_{ab} accounts for photon absorption in the target material. It was calculated using the photon cross sections of Storm and Israel [23] by assuming that the muon stops occurred at the target center, and that the capture γ rays traversed half the target thickness. These assumptions were justified as the photon absorption corrections were small, C_{ab} varying from 0.92 to 1.00. Furthermore, if the muon stops were actually weighted towards the target front or rear, because GeA and GeB view opposite target faces, the resulting under- or over-estimation of C_{ab} would largely cancel in the average of the Ge detector yields.

The correction factor C_{sv} accounts for the "self-vetoing" of Ge detector signals. Self-vetoing occurs if a valid signal from GeA (GeB) is rejected by a veto signal from CSA (CSB). The veto signal from the Compton suppressor may be a prompt coincidence due to a γ-ray cascade in the daughter nucleus, a delayed coincidence due to a preceding muonic x ray, or a random coincidence due to accelerator, cosmic, or other backgrounds. The extent of self-vetoing is therefore dependent on the particular γ ray or x ray. To determine the self-veto correction factors C_{sv} we measured, for each γ ray or x ray, the ratio of counts (r) in the GeA (GeB) singles spectrum and the GeA·$\overline{\text{CSB}}$ (GeB·$\overline{\text{CSA}}$) coincidence spectrum. Assuming (i) no angular correlations between radiation detected in GeA (GeB) and CSB (CSA) and (ii) equal acceptances for the two suppressors, r is the self-veto loss and $(1 - r)$ is the self-veto correction. In practice, using the coincident 1.17 and 1.33 MeV γ rays from a ^{60}Co source, we corrected for the different CSA and CSB acceptances at ~ 1 MeV, and only assumed equal energy dependences for the CSA and CSB acceptances. Since the correction factors C_{sv} were quite small, C_{sv} ranging from 1.00 to 1.20, these assumptions were justified. Also, for a few γ-ray lines the GeA·$\overline{\text{CSB}}$ (GeB·$\overline{\text{CSA}}$) coincidence spectra statistics were insufficient to determine r, and we simply employed an average value of C_{sv}.

[1] M. L. Goldberger and S. B. Treiman, Phys. Rev. **110**, 1178 (1958).

[2] V. Bernard, N. Kaiser, and U-G. Meißner, Phys. Rev. Lett. **69**, 1877 (1992).

[3] M. Ericson, A. Figureau, and C. Thévenet, Phys. Lett. **45B**, 19 (1973).

[4] J. Delorme, M. Ericson, A. Figureau, and C. Thévenet, Ann. Phys. (N.Y.) **102**, 273 (1976).

[5] J. Delorme and M. Ericson, Phys. Rev. C **49**, 1763 (1994).

[6] M. Rho, Annu. Rev. Nucl. Part. Sci. **34**, 531 (1984).

[7] T. P. Gorringe, B. Johnson, J. Bauer, M. Kovash, R. Porter, D. S. Armstrong, M. D. Hasinoff, D. F. Measday, B. A. Moftah, and D. H. Wright, Phys. Rev. Lett. **72**, 3472 (1994).

[8] B. Johnson, T. P. Gorringe, J. Bauer, M. Kovash, R. Porter, D. S. Armstrong, M. D. Hasinoff, D. F. Measday, B. A. Moftah, and D. H. Wright, Phys. Rev. C **54**, 2714 (1996).

[9] G. H. Miller, M. Eckhause, F. R. Kane, P. Martin, and R. E. Welsh, Phys. Rev. Lett. **29**, 1194 (1972).

[10] V. Brudanin, V. Egorov, A. Kachalkin, V. Kovalenko, A. Salamatin, I. Stekl, V. Vorobel, Ts. Vylov, I. Yutlandov, Sh. Zaparov, J. Rak, S. Vassiliev, J. Deutsch, R. Prieels, L. Grenacs, and Ch. Briancon, Nucl. Phys. **A587**, 577 (1995).

[11] B. A. Moftah, E. Gete, D. F. Measday, D. S. Armstrong, J. Bauer, T. P. Gorringe, B. L. Johnson, B. Siebels, and S. Stanislaus, Phys. Lett. B **395**, 157 (1997).

[12] K. Junker, V. A. Kuz'min, A. A. Ovchinnikova, and T. V. Tetereva, WEIN '95, IVth International Symposium on Weak and Electromagnetic Interactions in Nuclei, Osaka, 1995, p. 394.

[13] D. S. Armstrong, J. Bauer, T. P. Gorringe, B. L. Johnson, S. Kalvoda, R. Porter, B. Siebels, B. A. Moftah, E. Gete, D. F. Measday, and S. Stanislaus, Hyperfine Interact. **103**, 169 (1996).

[14] N. Mukhopadhyay, Phys. Rep., Phys. Lett. **30C**, 1 (1977).

[15] A. Olin, P. R. Poffenberger, and D. I. Britton, Nucl. Instrum. Methods Phys. Res. **222**, 463 (1984).

[16] P. Vogel, Phys. Rev. A **22**, 1600 (1980).

[17] L. F. Mausner, R. A. Naumann, J. A. Monard, and S. N. Kaplan, Phys. Rev. A **15**, 479 (1977).

[18] F. J. Hartmann, T. von Egidy, R. Bergmann, M. Kleber, H.-J. Pfeiffer, K. Springer, and H. Daniel, Phys. Rev. Lett. **37**, 331 (1976).

[19] F. J. Hartmann, R. Bergmann, H. Daniel, H.-J. Pfeiffer, T. von Egidy, and W. Wilhelm, Z. Phys. A **305**, 189 (1982).

[20] D. Kessler, H. Mes, A. C. Thompson, H. L. Anderson, M. S. Dixit, C. K. Hargrove, and R. J. McKee, Phys. Rev. C **11**, 1719 (1975).

[21] R. R. Kinsey, computer code NUDAT, National Nuclear Data Center, Brookhaven National Laboratory, Upton, NY, 1996.

[22] P. M. Endt, Nucl. Phys. **A521**, 1 (1990). P. M. Endt and J. G. L. Booten, *ibid.* **A555**, 499 (1993).

[23] E. Storm and H. I. Israel, Nucl. Data, Sect. A **7**, 565 (1970).

[24] T. Suzuki, D. F. Measday, and J. P. Roalsvig, Phys. Rev. C **35**, 2212 (1987).

[25] T. P. Gorringe, B. Johnson, J. Bauer, M. Kovash, R. Porter, P. Gumplinger, M. D. Hasinoff, D. F. Measday, B. A. Moftah, D. S. Armstrong, and D. H. Wright, Phys. Lett. B **309**, 241 (1993).

[26] J. G. Congleton, Phys. Rev. A **48**, R12 (1993).

[27] L. B. Egorov, C. V. Zhuravlev, A. E. Ignatenko, A. V. Kuptsov, Li Hsuan-ming, and M. G. Petrashku, Sov. Phys. JETP **14**, 494 (1962).

[28] J. F. Lathrop, R. A. Lundy, V. L. Telegdi, and R. Winston as discussed in R. Winston, Phys. Rev. **129**, 2766 (1963).

[29] R. Winston, Phys. Rev. **129**, 2766 (1963).

[30] T. J. Stocki, Ph.D. thesis, University of British Columbia, 1998.

[31] G. H. Miller, M. Eckhause, P. Martin, and R. E. Welsh, Phys. Rev. C **6**, 487 (1972).

[32] T. A. E. C. Pratt, Nuovo Cimento B **LXI B**, 119 (1969).

[33] M. Morita and A. Fujii, Phys. Rev. **118**, 606 (1960).

[34] J. D. Walecka, *Semi-leptonic Weak Interactions in Nuclei, in Muon Physics*, edited by C. S. Wu and V. Hughes (Academic, New York, 1975); J. D. Walecka, *Theoretical Nuclear and Subnuclear Physics* (Oxford, New York, 1995).

[35] B. A. Brown and B. H. Wildenthal, At. Data Nucl. Data Tables **33**, 347 (1985).

[36] B. A. Brown, A. Etchegoyen, W. D. M Rae, and N. S. Godwin, The Oxford-Buenos-Aires-MSU shell model code (OXBASH), MSUCL Report No. 524, 1986.

[37] B. A. Brown and B. H. Wildenthal, Annu. Rev. Nucl. Part. Sci. **38**, 29 (1988).

[38] Ya. B. Zel'dovich and S. S. Gershtein, Sov. Phys. JETP **2**, 567 (1957).

[39] R. P. Feynman and M. Gell-Mann, Phys. Rev. **109**, 193 (1958).

[40] S. Weinberg, Phys. Rev. **112**, 1375 (1958).

[41] J. C. Sens, Phys. Rev. **113**, 679 (1958).

[42] G. Ravenhall, as discussed in J. D. Walecka, *Semi-leptonic Weak Interactions in Nuclei* [34].

[43] K. Schreckenbach, P. Liaud, R. Kossakowski, H. Nastoll, A. Bussiere, and J. P. Guillaud, Phys. Lett. B **349**, 427 (1995).

[44] T. Siiskonen, J. Suhonen, V. A. Kuz'min, and T. V. Tetereva, Nucl. Phys. **A635**, 446 (1998); **A651**, 437 (1999).

[45] C. D. Goodman, C. A. Goulding, M. B. Greenfield, J. Rapaport, D. E. Bainum, C. C. Foster, W. G. Love, and F. Petrovich, Phys. Rev. Lett. **44**, 1755 (1980).

[46] K. P Jackson, A. Celler, W. P. Alford, K. Raywood, R. Abegg, R. E. Azuma, C. K. Campbell, S. El-Kateb, D. Frekers, P. W. Green, O. Hausser, R. L. Helmer, R. S. Henderson, K. H. Hicks, R. Jeppesen, P. Lewis, C. A. Miller, A. Moalem, M. A. Moinester, R. B. Schubank, G. G. Shute, B. M. Spicer, M. C. Vetterli, A. I. Yavin, and S. Yen, Phys. Lett. B **201**, 25 (1988).

[47] W. P. Alford and B. M. Spicer, *Advances in Nuclear Physics*, Vol. 24 (Plenum, New York, 1998).

[48] B. Siebels, T. P. Gorringe, W. P. Alford, J. Bauer, J. Evans, S. El-Kateb, K. P. Jackson, A. Trudel, and S. Yen, Phys. Rev. C **52**, 1488 (1995).

[49] B. D. Anderson, N. Tamimi, A. R. Baldwin, M. Elaasar, R. Madey, D. M. Manley, M. Mostajabodda'vati, J. W. Watson, W. M. Zhang, and C. C. Foster, Phys. Rev. C **43**, 50 (1991).

[50] R. M. Sedlar, T. P. Gorringe, W. P. Alford, D. A. Beatty, J. Campbell, H. T. Fortune, P. Hui, D. A. Hutcheon, R. B. Ivie, K. P. Jackson, A. G. Ling, Z. Mao, M. G. McKinzie, B. Siebels, D. A. Smith, P. Walden, and S. Yen, Phys. Rev. C **59**, 789 (1999).

[51] B. D. Anderson, T. Chittrakarn, A. R. Baldwin, C. Lebo, R. Madey, P. C. Tandy, J. W. Watson, C. C. Foster, B. A. Brown, and B. H. Wildenthal, Phys. Rev. C **36**, 2195 (1987).

[52] T. Siiskonen, J. Suhonen, and M. Hjorth-Jensen, Phys. Rev. C **59**, 1839 (1999).